SMOSops Scientific Support Study

(CCN-2 to SMOSops ESTEC contract 20946/07/NL/FF)

Task 2: Secondary Payloads Science Assessment

(Contract ECE-C0-B-08-505)

Final Report

Marcos Portabella, Roberto Sabia, Jordi Font, Adriano Camps
SMOS-BEC (CSIC-UPC), Barcelona
and
Nicolas Reul
IFREMER, Brest

Barcelona, July 2009

SMOSops Scientific Support Study

Task 2: Secondary Payloads Science Assessment

Final Report

INTRODUCTION

SMOSops will introduce several technological modifications to provide an improved determination of soil moisture and ocean salinity from space. It is proposed to measure H and V polarisations in parallel, a good approach since it increases radiometric sensitivity with respect to the present SMOS set up. A fully populated hub will provide better measurement of the short baselines, also a very good approach since it allows redundancy to improve error correction and robustness. Longer arms will lead to improved spatial resolution. A reduced spacing between antenna elements will improve the swath and revisit time by enlarging the alias free field of view, while the Flat Target correction can cope with the increase of antenna coupling due to the reduced spacing.

The main geophysical source of error in the determination of sea surface salinity is the impact of surface roughness. The L-band emissivity of a flat sea (as function of temperature, salinity, viewing angle and polarization) is quite well modelled, but the different processes that impact on the emission of a roughened surface are not fully described or considered in the several theoretical formulations available until now. However, it is critical to know the changes in the ocean brightness temperature produced by the sea state as they can be even larger than the salinity-induced change itself. In the case of SMOS the incomplete formulation of this effect is accompanied by another drawback: there is no independent measurement of parameters able to describe the surface roughness (wind vector, significant wave height, mean surface slope, radar backscatter ...) collocated with the radiometric data acquisition, and then we have to rely on numerical forecasts to provide this information to the salinity retrieval algorithm.

SMOSops envisages the use of two additional payloads to face this problem: an X-band Fully Polarimetric Interferometric Radiometer (FPIR) and a Global Navigation Satellite Systems Reflectometry (GNSS-R) instrument. They are expected to be able to provide simultaneous information on the sea surface roughness and, in an extent to be determined, reduce the impact of the roughness effect uncertainty in the modelled brightness temperature, and hence in the salinity retrieval.

In spring 2008 ESA concluded that within the on-going SMOSops contract that is defining the technology and the basic architecture of the MIRAS instrument based on the experience gained in SMOS, there were important system aspects of the SMOSops mission that go beyond technological issues and require scientific support. This includes the optimum orbital altitude, instrument tilt and steering angles, and the benefits of the additional payloads, as well as the need to implement some RFI mitigation techniques. A Statement of Work "SMOSops Scientific Support Study"

(CCN-2 to SMOSops) was issued in May 2008, addressed to several SMOS Expert Support Laboratories. This SoW included among others:

Task 2 – Secondary Payloads Science Assessment to analyse the benefits of the two additional payloads (GNSS-R and FPIR) in ocean salinity retrievals.

This activity was specifically assigned to ICM-CSIC. The SoW indicates that the following documentation has to be used as input:

[RD-2]: Yan J., "FPIR: a One-Dimensional Full Polarisation Interferometric Radiometer", CSSAR -CAS Report, September 2007.

[RD-3]: Garrison J.L., Komjathy A., Zavorotny V.U., Katzberg S.J., "Wind Speed Measurements Using Forward Scattered GPS Signals", TGARS, Vol. 40, No. 1, January 2002, pp. 50-65.

[RD-4]: Cardellach E., Rius A., "Sea Surface Slopes PDF from GNSS Reflected Signals", IGARSS-2007 Proceedings, Barcelona, Spain, July 2007.

[RD-5]: Gleason S.T., "Reflecting on GPS", GPS World, Innovation Column, October 2007, pp. 44-49.

and states:

Two sensors are proposed to be embarked on SMOSops: an X-band Fully Polarimetric Interferometric Radiometer (FPIR) and an experimental GNSS Reflectometry (GNSS-R) payload.

a) FPIR

FPIR is sensitive to the capillary waves formed on the sea surface by the wind [RD-2]. Therefore FPIR will measure the wind, from which the sea surface roughness at the scales which affect the L-band brightness temperature have to be derived.

The contractor shall review whether the frequency selected for FPIR (X-band) is the optimum one. Only bands with primary allocation for remote sensing shall be considered in such trade-off. Bands with shared or secondary allocation shall not be studied. The contractor shall furthermore trade off a dual polarisation X-band instrument against a full polarisation one, as the former would bring considerable hardware implementation advantages.

b) GNSS-R

GNSS-R is sensitive to the mean squared slope of the surface, that is, to the roughness directly [RD-3-4-5]. However, by the time SMOSops flies, it is unclear how many GNSS satellites (thus reflected points) there will be available, coverage becoming an issue. An optimistic scenario is one where GALILEO is operational, and GLONASS is transmitting TDMA-modulated signals, in addition to the GPS system. Then some 12 reflected points would be available on average within the SMOSops field of view, providing enough sampling density for roughness corrections. The present situation is that only the GPS signals are available and suited for GNSS-R, which would give 4 reflections, a somewhat too sparse coverage.

The contractor shall estimate the expected number and distribution of GNSS reflections available for the GNSS-R payload in the timeframe of SMOSops. The contractor shall establish the benefits of this payload for sea surface roughness corrections to the brightness temperatures. The contractor shall propose a method to process the GNSS-R data and the scientific output which is required. A trade-off between second and four order slope moments shall be provided as optimum output variable for surface roughness correction, or else, any alternative method.

Further benefits or added applications to the mission due to the additional payloads, FPIR and GNSS-R, shall be identified and preliminary studied as well by the contractor.

The output of this activity has to be a Report on Science Assessment of the Secondary Payloads in SMOSops. This is the report we are presenting here. It is organised in two separate sections: FPIR lead by M. Portabella and GNSS-R lead by R. Sabia.

SMOSops Scientific Support Study

Secondary Payloads Science Assessment - FPIR

At L-band, the brightness temperature (Tb) over the ocean is mainly modulated by three geophysical variables: the sea surface salinity (SSS), the sea surface temperature (SST), and the sea surface roughness. The latter produces large deviations in Tb from the flat sea model (Font et al., 2004). Moreover, analysis of pre-launch semi-empirical geophysical model functions shows that sensitivities to surface roughness and SSS are of the same order (Gabarró et al., 2009). As such, additional information on the sea surface roughness is essential for an L-band radiometer to meet the SSS accuracy requirements (i.e., 0.1 psu for monthly 2º x 2º gridded SSS product). Unlike Aquarius, which carries a scatterometer for roughness estimation as secondary payload, SMOS will only carry an L-band radiometer (i.e., Microwave Imaging Radiometer by Aperture Synthesis – MIRAS) (Martín-Neira and Goutoule, 1997) and therefore will have to rely on auxiliary roughness information to obtain the best estimate of SSS. The auxiliary data uncertainty may prevent SMOS SSS retrievals to meet the already mentioned accuracy requirements.

As part of the preliminary activities for SMOSops, i.e., the SMOS follow-on, the Chinese Centre for Space Science and Applied Research (CSSAR) has offered to launch together with MIRAS an X-band fully (or dual) polarized conical antenna beam radiometer, i.e., the Fully Polarimetric Interferometric Radiometer – FPIR (Yan et al., 2007; Yan, 2008) to estimate sea surface roughness at about 100-km resolution.

The initial goals of this study, as defined in the Statement of Work (SMOSops Scientific Support Study, CCN-2 to SMOSops, ESTEC, 25 May 2008), were to review whether the frequency selected for FPIR (X-band) is the optimum one and whether full-pol mode is strictly necessary. Only bands with primary allocation for remote sensing shall be considered in such trade-off. Bands with shared or secondary allocation shall not be studied. This study shall trade off a dual polarisation X-band instrument against a full polarisation one, as the former would bring considerable hardware implementation advantages.

Furthermore, the study has been extended to account for several other aspects in the FPIR configuration which may have a significant impact in the optimization of the SMOSops SSS retrievals. These include the incidence angle configuration, the dual frequency consideration, and the spatial resolution.

1. FPIR radiometric sensitivities

To improve SSS retrieval accuracy from SMOSops, it is important to assess FPIR's ability to provide accurate information on the sea surface roughness induced emissivity. Besides sea surface roughness, there are other geophysical parameters, such as SST, water vapour (WV), cloud liquid water (CLW), and rain that modulate Tb measurements of a microwave passive system. As such, it is important to assess the relative contributions of all these parameters to Tb (sensitivities) at X-band and

neighbouring bands, notably at C-band for its proximity to L-band. In this section, the pre-defined FPIR incidence angle of 50° is considered. Note that past and current radiometers onboard satellites have fixed incidence angles of about 50°-55°. From these, the Windsat radiometer and the AMSR-E onboard Aqua contain multiple channels, including C-band, X-band and higher frequencies. As such, publications related to these systems are indeed very relevant and reviewed in the framework of this study.

1.1 Wind speed effects

Assuming that the sea surface wind speed is a good proxy for the sea surface roughness, we first take a look at Tb sensitivities to wind speed for X and neighbouring bands.
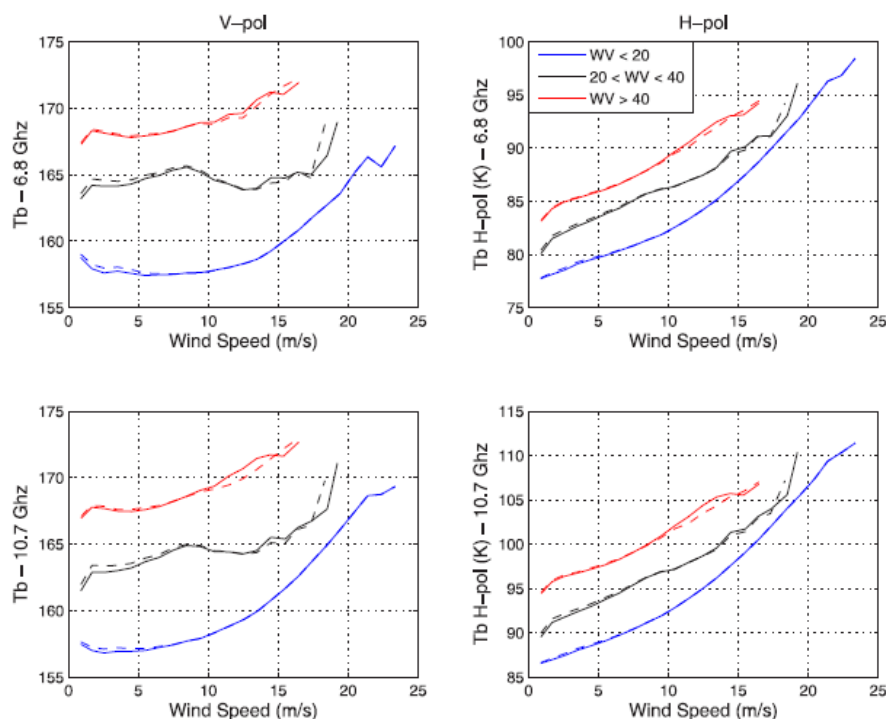

Figure 1. Windsat mean V-pol (left panels) and H-pol (right panels) Tb's binned as a function of ECMWF wind speed (m/s), at 6.8 GHz (top) and 10.7 GHz (middle) and for different integrated water vapor ranges: 0 mm < WV < 20 mm (blue lines), 20 mm < WV < 40 mm (black lines), and 40 mm < WV < 60 mm (red lines). WindSat (solid lines) and Jason microwave radiometer (dashed lines) integrated water vapor data are used [Figure 6 of Quilfen et al., 2007].

Figure 1 (Quilfen et al., 2007) displays the Windsat mean Tb values as a function of collocated European Centre for Medium-range Weather Forecasts (ECMWF) wind speeds, for different WV intervals estimated by Windsat (solid) and collocated Jason Microwave Radiometer (JMR) measurements (dashed), and for different bands and polarizations. It is clear that very similar results are obtained regardless of whether the WV data source is Windsat or JMR, therefore indicating the reliability of the presented results. Moreover, Quilfen et al. (2007) also show that very similar curves are also obtained when using collocated QuikSCAT scatterometer winds instead of ECMWF winds as reference.

In general, Figure 1 shows that the sensitivity to wind speed increases with frequency and is remarkably larger for horizontal polarization (right panels) than for vertical (left panels). More details on the horizontally polarized Tb (TbH) sensitivities to wind speed are shown in Figure 2 (see regression lines) and Table 1. [Note that similar results are obtained for the vertically polarized Tb (TbV) sensitivities (not shown)]. The Tb sensitivity to wind speed is about 10-25% larger for X-band than for C-band (see Table 1).
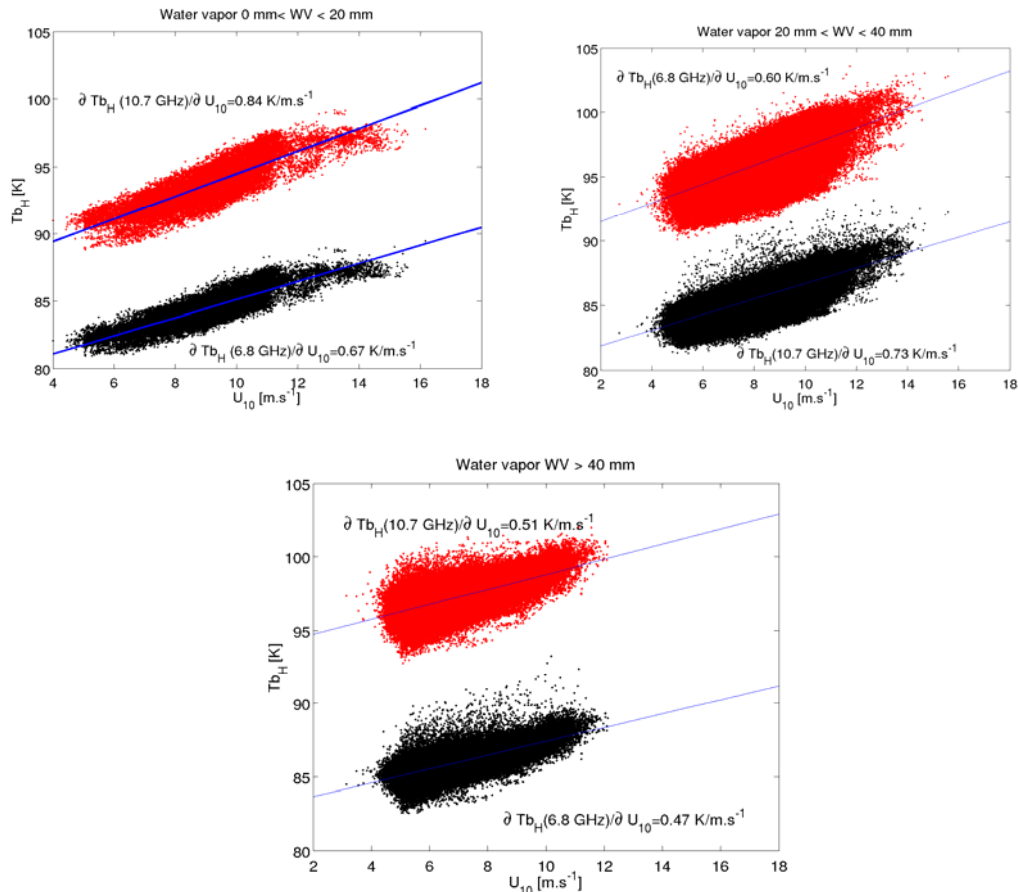

Figure 2. Windsat C-band (black) and X-band (red) H-pol Tb's as a function of ECMWF wind speed for different Windsat-derived water vapour ranges. The regression lines indicate Tb sensitivity to wind speed. [Adapted from Quilfen et al., 2007]

Integrated Water Vapor	X-band (10.7 GHz)	C-band (6.8 GHz)
<20 mm	0.84	0.67
20< <40 mm	0.73	0.60
> 40 mm	0.51	0.47

Table 1: Averaged Wind speed sensitivity of Windsat C and X-band H-pol Tb derived from the regression lines of Figure 2. [Adapted from Quilfen et al., 2007]

1.2 Wind direction effects

The Tb sensitivity to wind direction has been thoroughly studied and quantified for Windsat X-band and higher frequency channels (e.g., Yueh et al., 2006; Quilfen et al., 2007). The third (U) and fourth (V) stokes parameters are sensitive to wind direction

and are little affected by atmospheric effects (Yueh et al., 2006). The azimuthal modulation increases with wind speed up to 18 m/s and does not vary significantly beyond 20 m/s (Quilfen et al., 2007) In line with this, Yueh (2008) shows that, for X-band and after proper atmospheric correction, the wind direction signal is maintained up to 50 m/s. However, the azimuthal modulation is too small to derive any reliable wind direction information below 7-8 m/s (Freilich and Vanhoff, 2006; Monaldo, 2006; Soisuvarn et al., 2007). Regarding C-band, although no satellite microwave system has ever carried a fully polarimetric C-band channel, the U and V wind direction signal is believed to be lower than for X-band.

In general, Tb_V and Tb_H are as sensitive to wind direction as U and V (Yueh et al., 1999; Meissner and Wentz, 2002). However, their sensitivity to inhomogeneous cloud covers overwhelms their wind directional dependence (Yueh et al., 2006). The wind direction signal decreases with decreasing frequency, being 60% smaller for X-band and (about) 80% smaller for C-band as compared with the 37 GHz channel (Meissner and Wentz, 2002). As for U and V, the wind direction signal for Tb_V and Tb_H increases with wind speed, reaching a significant 3 k peak to peak modulation, which may lead to up to 4 m/s errors in wind speed, for winds above 15 m/s at 18.7 GHz (Meissner and Wentz, 2006). However, the modulation at high winds is reduced about 80% at X-band and furthermore at C-band. As such, not accounting for wind direction leads to generally small wind speed retrieval errors at X-band and especially at C-band.

1.3 WV effects

It is already clear from Figure 2, that the red dots present a larger scatter than the black dots, indicating that X-band is also more sensitive to WV than C-band. The regression lines in Figure 3 indicate that X-band is around twice more sensitive to WV than C-band for a large portion of the wind speed spectrum (winds below 7 m/s).
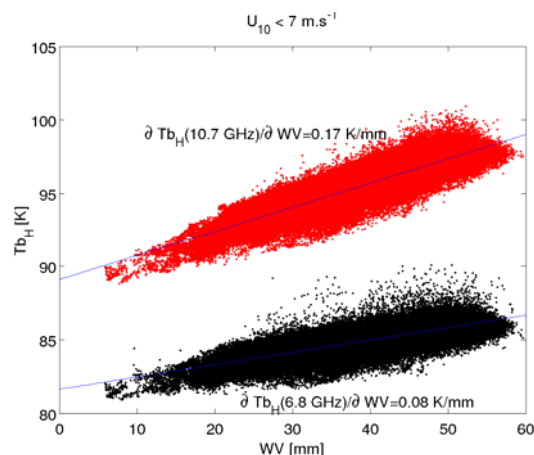

Figure 3. Windsat C-band (black) and X-band (red) H-pol Tb's as a function of Windsat-derived water vapour for ECMWF winds below 7 m/s. The regression lines indicate Tb sensitivity to water vapour. [Adapted from Quilfen et al., 2007]

It is also clear from Figures 1 and 2, that the Tb sensitivity to wind speed decreases with WV content (see curves' slopes for the different WV intervals), i.e., as the WV content in the atmosphere increases, the signal coming from the surface (emissivity)

decreases. This attenuation will in turn negatively impact the estimation of sea surface roughness.

1.4 CLW and rain effects

As discussed in Meissner and Wentz (2008), similar to WV, CLW and rain are known to increase the atmospheric attenuation of microwave signals (especially at high frequencies) and, as such, to decrease the sensitivity of microwave passive instruments to sea surface roughness. In line with WV effects, the Tb sensitivity to CLW content and rain increases with frequency, such that high frequency channels, e.g., 18 GHz, 23 GHZ, and/or 37 GHz, have been traditionally used for rain detection and/or retrievals (Adams et al., 2005; 2006; Bettenhausen et al., 2006).
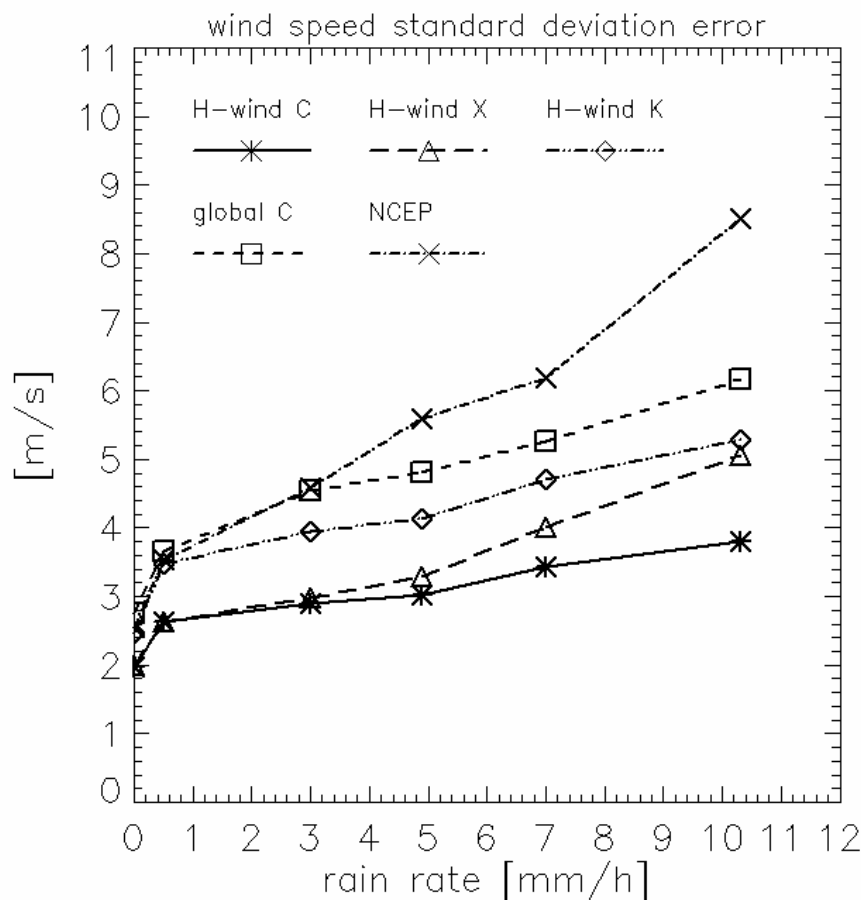

Figure 4. Estimated standard deviation error of the wind speed retrievals in rain as function of surface rain rate: WindSat H-wind algorithm utilizing C-band and higher frequencies (solid line and stars), WindSat H-wind algorithm utilizing X-band and higher frequencies (long dashed line and triangles), WindSat H-wind algorithm utilizing K-band and higher frequencies (dashed-dot-dot lines and diamonds), WindSat global wind speed algorithm utilizing C-band and higher frequencies (short dashed lines and squares), NCEP GDAS (dashed – dot lines and crosses). The figure shows the RMS of the difference between the various measurements and the scaled and resampled HRD winds [m/s]. The surface rain rates [mm/h] are derived from WindSat measurements [Figure 11 from Meissner and Wentz, 2008].

Meissner and Wentz (2008) estimate the accuracy of several wind retrieval algorithms over rainy conditions based on different Windsat channel combinations. Figure 4

(Meissner and Wentz, 2008) shows the wind speed retrieval error of several algorithms: a global algorithm using C-band + higher frequencies, and three other algorithms specifically developed for rainy conditions, i.e., C-band + higher frequencies, X-band + higher frequencies, and K-band + higher frequencies. The National Center for Environmental Prediction (NCEP) model winds are also plotted. The standard deviations (errors) are computed against NOAA's Hurricane Research Division (HRD) winds, i.e., wind field information derived from ground observations (buoys, ships), aircraft observations, and satellite data (QuikSCAT, ERS, SSM/I, TMI, GOES). Figure 4 shows the benefits of including low frequency channels to improve wind speed accuracy for increasing rain rates. In particular, the inclusion of C-band has a substantially positive impact in the wind speed retrieval quality for moderate and heavy rain (above 7 mm/h). This is also the case for global algorithms (not shown).

1.5 SST effects

As already discussed, the sensitivity to WV also increases with frequency. However, when comparing Figure 1a to Figure 1c, the Tb_V sensitivity to WV, as denoted by the separation between curves, seems to be higher at C-band than at X-band. This is caused by the large C-band sensitivity to SST, which is usually correlated with the integrated WV in the atmosphere. The Tb_V sensitivity to SST decreases with frequency, reaching at K-band (18.7 GHz) only half of that at C-band (Quilfen et al., 2007). As shown in Gentemann et al. (2009), this decrease is true for cold waters (below 15°C). However, the SST sensitivities at C and X-band are very similar in warm waters.

1.6 Foam effects

As seen in Figures 1a and 1c, Tb_V is rather insensitive to wind speed except for high winds. Indeed, at around 50°-55° incidence angle, the V-pol signal is little sensitive to sea surface roughness. The change in V-pol is essentially due to the presence of foam, whose coverage increases exponentially with wind speed (e.g., Monahan and O'Muircheartaigh, 1986). However, the modelling of foam induced emissivity is still immature (Camps et al., 2005). Quilfen et al (2007) question the validity of several models (English and Hewison, 1998; Deblonde, 2000; Kudryavtsev et al., 2003), which account for emissivity from foam patches, notably at very high winds (above 25 m/s).

1.7 Incidence angle effects

As mentioned at the beginning of section 1, the FPIR sensitivities are reviewed for a fixed incidence angle of about 50°, since this is the FPIR preliminary configuration and past and current satellite microwave radiometers have used a very similar incidence angle configuration.

The sea surface roughness impact on microwave emissivity at 0° is not the same than at 50°, because downward looking radiometers are sensible to different scales of

surface waves as a function of incidence angle. Typically, around nadir and for low incidences, surface roughness wavelengths of the order of the electromagnetic (EM) wavelength (i.e., ~21 cm at L-band, ~5cm at C-band, ~3cm at X-band) will be the dominant contributors to the roughness impact on emissivity. As the incidence angle increases, larger waves start to play an increasing role in the contribution and at around 50°, both scales of the order of the EM wavelength and larger waves will have an impact. Since MIRAS is a multi-incidence instrument with incidences ranging from 0° to 60/70°, the incidence angle definition for FPIR shall be carefully examined (as function of FPIR frequency), so that the final nominal choice (currently understood to be chosen at 50°) allows the sensing of most surface scales dominantly responsible for roughness excess emissivity at L-band, from 0° to 60°. In other words, a FPIR with multiple incidence angles will certainly result in a more complementary instrument to MIRAS than a FPIR with a single incidence angle (i.e., 50°).

2. SMOSops SSS retrieval strategies

In this section, we present two different SSS retrieval strategies, the selection of which may have an impact on the FPIR design.

2.1 Multi-parameter inversion

Similar to SMOS, the SMOSops retrieval procedure may be based on the inversion of all the geophysical parameters, which influence the Tb measurements. As discussed in section 1, MIRAS and FPIR Tb's are modulated by SSS, SST, sea surface roughness, and atmospheric effects (WV, CLW, rain). Alternatively, sea surface roughness can be estimated by inverting FPIR measurements only (i.e., a multi-parameter inversion of SST, roughness, and atmospheric effects) and then used as a constraint on the MIRAS Tb inversion to retrieve SSS.

Regarding the multi-parameter inversion strategy, several cost function configurations have already been proposed and assessed (with simulations) for SMOS (Camps et al., 2003, 2005; Zine et al., 2008; Gabarró et al., 2009), in which the wind speed is used as a proxy for sea surface roughness induced emissivity. As such, FPIR derived sea surface wind information can be used to better constrain the SSS retrievals from SMOSops. The main advantage of this method is that FPIR derived information (wind and atmospheric parameters) can be easily validated and monitored.

However, this approach has the following limitations:

a) The sea surface induced emissivity is not only driven by sea surface wind. Quilfen et al. (2007) show that the correlation between Tb and wind decreases with wind speed. Among other effects, such as variability of wind and waves, at moderate to high winds, the presence of foam plays an important role in the emissivity, which is not yet fully understood, as already mentioned in section 1.6.

b) By increasing the number of parameters in the inversion (i.e., atmospheric effects are considered marginal at L-band, but not at the higher frequencies in which FPIR will operate), the SSS retrieval becomes more challenging. For

instance, new parameters have to be modelled and their possible non-linear dependencies may cause systematic errors in the inversion process.

2.2 Roughness effect reduction by channel combination

Meissner and Wentz (2002; 2006) show that by combining Tb_V and Tb_H, one can substantially reduce the sensitivity (at various frequencies) to atmospheric effects by preserving the sensitivity to wind speed up to 8 m/s. Furthermore, Meissner and Wentz (2008) show that by combining C-band and X-band channels, one can reduce rain effects by preserving most of the wind speed sensitivity up to extreme wind conditions. Figure 5 (Meissner and Wentz, 2008) shows the benefits of a multiple frequency combination (solid curve) as compared to a single frequency H-pol/V-pol combination (dashed curve). While the multiple frequency combination (solid) is slightly less sensitive to wind speed than the X-band H-pol (dashed-dot-dot), the former is substantially less sensitive to rain than the latter (not shown).
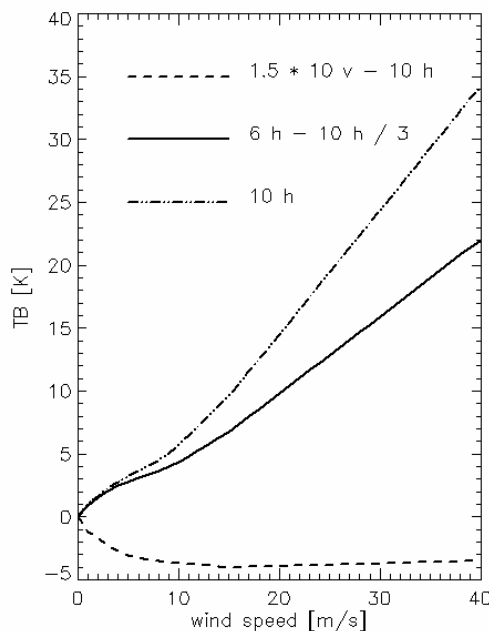

Figure 5. Top of the atmosphere brightness temperature [Kelvin] calculated in Meissner and Wentz (2008) as function of wind speed for various channel combinations: 10h (dashed-dot-dot), 1.5 * 10v − 10h (dashed), 6h - 1/3*10h (solid), where 6h, 10h, and 10v correspond to C-band/H-pol, X-band/H-pol, and X-band/V-pol channels, respectively. For computing the curves we have used an effective temperature of 10°C and a surface rain rate of 5 mm/h [Figure 9 from Meissner and Wentz, 2008].

The concept of multiple channel combination could also be adopted for improving SMOSops SSS retrievals, i.e., MIRAS and FPIR measurements may be optimally combined to reduce sea surface roughness effects while preserving L-band SSS sensitivity. In line with this, Reul et al. (2009) have recently shown that by combining AMSR-E C- and X-band Tb's, the roughness effect is substantially reduced and an SSS signal can be derived from averaged (monthly) products [Note that atmospheric effects are filtered out using AMSR-E higher frequency channels]. This is particularly important since SSS sensitivity at C and X-band is about one order of magnitude smaller than that at L-band.

As already discussed in section 1.7, due to the large range of MIRAS incidence angles (0°-60°), a multiple incidence angle FPIR instrument is however needed. The main advantage of this strategy is that the SSS retrieval problem is reduced to the inversion of two parameters, i.e., SSS and SST.

The main limitations are:

a) In every observation cell, where MIRAS viewing geometry is variable, i.e., multiple measurements at different incidence and azimuth angles, FPIR viewing geometry needs to be complementary. This poses a real challenge since the channel combination regression may become quite complex. For example, under light wind condition, the surface roughness scales resolved at C or X-band may not be perfectly correlated with the scales resolved at L-band.

b) In contrast with L-band, C-band and (notably) X-band are sensitive to atmospheric effects. As such, the channel combination will have to reduce (or ideally remove) both roughness and atmospheric effects, while preserving SSS sensitivity.

3. Discussion on possible FPIR configurations

Given the Tb sensitivities review presented in section 1 and the SSS retrieval strategies discussed in section 2, several relevant FPIR configurations in terms of frequency, polarization and incidence angle will be discussed in this section.

3.1 Single frequency

The optimal frequency to complement the MIRAS L-band should ideally be most sensitive to sea surface roughness and little sensitive to other geophysical parameters, notably the atmospheric parameters. However, as discussed in section 1, the sensitivities to both the sea surface roughness and the atmosphere generally increase with frequency.

As compared to C-band, X-band is about 20% more sensitive to sea surface roughness but almost twice as sensitive to atmospheric effects. As mentioned in section 2.2, the combination of V-pol and H-pol measurements (Tb_V and Tb_H) to reduce atmospheric effects while preserving the sensitivity to roughness does not work for X-band at high winds (Meissner and Wentz, 2002; 2006). Although not thoroughly tested, this polarization combination is believed to work even less for C-band since wind speed sensitivity is lower than for X-band.

At higher frequencies than X-band, e.g., 18 GHz, 22 GHz, or 37 GHz channels, higher roughness sensitivity is expected for "dry" atmospheres. However, a large amount of observations would have to be filtered out due to "atmospheric contamination".

Another relevant aspect of the FPIR frequency is its proximity to L-band. When the wind starts to blow over the ocean, the gravity-capillary waves (centimetric) are

formed almost instantaneously. Part of the energy of the wind is absorbed by the ocean and transferred in space and time from the shorter waves (gravity-capillary) to the gravity (decimetric) and longer (metric or larger) waves. As such, in areas where the sea state is not in equilibrium with the local wind, such as low wind areas, fetch, and areas of high spatial and temporal variability (frontal areas, vicinity of low-pressure centres), the sea surface roughness at L-band scales may not be correlated with the sea surface roughness at C-band scales. This decorrelation effect increases as the frequency gap with respect to L-band increases, e.g., at X-band and higher frequencies. In other words, from the frequencies under study, C-band is expected to correlate better to L-band.

Another relevant aspect of the frequency selection is the SST sensitivity. As discussed in section 1.5, the sensitivity to SST decreases with frequency. As such, C-band is more sensitive to SST than X-band. Although the primary objective of FPIR is to accurately characterize the sea surface roughness, given the L-band MIRAS sensitivity to SST, a frequency that can also resolve SST will in turn help to better constrain the SMOSops SSS retrievals.

3.2 Fully polarimetric channels

As discussed in section 1.2, U and V are essential to derive the sea surface wind direction or more importantly the sea surface roughness directional signatures (not always correlated with wind direction as discussed in section 2.1). However, the impact of a full-pol FPIR on SMOSops SSS retrievals is similar to that of a dual-pol FPIR due to the following:

a) As shown in several SMOS pre-launch campaigns, wind direction modulation at L-band is negligible, even in U and V (Camps et al, 2004; Sobjaerg et al., 2003).

b) As discussed in section 1.2, the wind direction signal in Tb_V and Tb_H is small at X-band and even smaller at C-band. As such, not accounting for directional signatures in the retrieval process, does not generally lead to significant errors in the roughness characterization of a dual-pol X or (notably) C-band system, except for high winds (see section 1.2).

c) To retrieve wind direction information from passive microwave systems with similar accuracy to that provided by, e.g., NWP models, at least 6 polarimetric channels are needed (Meissner and Wentz, 2006; Quilfen et al., 2007), which implies at least three different frequencies with polarimetric capabilities (e.g., Windsat and AMSR-E instruments). Moreover, as shown by Monaldo (2006) and Soisuvarn et al. (2007), the retrieved wind direction accuracy is only comparable to NWP output for winds above 7-8 m/s, and substantially decreases at low winds. As such, using auxiliary wind direction information is a good alternative to the polarimetric direction information for sea surface roughness estimation. Note that for non-polarimetric systems, such as SSM/I and TMI, auxiliary wind direction information (e.g., NWP output) is successfully used to retrieve wind speed (Wentz and Meissner, 2007).

3.3 Dual frequency

As discussed in section 1, a trade-off between sensitivity to roughness and sensitivity to atmospheric effects is required for a single-frequency FPIR. In section 2, polarization combinations are shown to reduce atmospheric sensitivity, although with limited success (e.g., below 8 m/s or for rainy conditions, roughness estimation accuracy substantially decreases). As also mentioned in section 2, in contrast with single frequency, dual frequency can substantially contribute to disentangle the effects of roughness and the atmosphere. In this section, we present the pros and cons of three different dual-frequency configurations:

a) C + X-band: These frequencies are the lowest under consideration and therefore the least affected by atmospheric effects. Moreover, they provide sufficient roughness sensitivity, and, as shown by Meissner and Wentz (2008), a combination of both frequencies results in accurate sea surface roughness estimation under "wet" atmospheres. However, as seen in Figure 4, the wind speed accuracy of a C+X (and higher frequencies) algorithm, specifically developed for rainy conditions, significantly decreases with rain rate.

b) X + 37 GHz: As discussed in section 1.4, K-band (18 GHz) and higher frequencies are used to retrieve and/or screen rain. The 37 GHz channel is particularly suitable for such purpose (Adams et al., 2005; 2006; Bettenhausen et al., 2006). Therefore, the 37 GHz can be used for filtering out (quality control) "atmospheric contaminated" data, i.e., data for which atmospheric effects substantially degrade the X-band channel's ability to accurately estimate sea surface roughness.

c) C + 37 GHz: As compared to b), this frequency combination would allow less data filtering (with the 37 GHz channel) due to atmospheric effects (C-band is less affected by atmosphere than X-band), at the expense of somewhat less accurate estimation of sea surface roughness under "dry" conditions (C-band is less sensitive to roughness than X-band).

The optimal frequency combination is at this time unclear, although it may depend on the SSS retrieval strategy discussed in section 2. If a multi-parameter retrieval approach is followed, the best estimate of wind speed as a proxy for sea surface roughness is sought. For such purpose, options b) or c) may be the optimal ones. On the other hand, if a frequency channel combination is used to remove (or substantially reduce) the sea surface roughness effect prior to SSS retrievals, C and X-band may provide a better proxy for the sea surface roughness measured at L-band. For example, the foam and rain splashing effects at L-band are in general better correlated with those at C and X-band than with those at 37 GHz.

3.4 Incidence angle

The advantages of a multi-incidence angle FPIR in the context of SMOSops have already been presented in previous sections. As already mentioned in section 2.2, the retrieval strategy based on channel combination would especially benefit from the multi-incidence angle concept. However, the complex viewing geometry of MIRAS makes the retrieval problem a real challenge.

One of the main problems of such FPIR configuration is that no passive radiometer with multiple incidence angle capability has ever operated in orbit. Therefore, to get an idea of the feasibility of such system in the context of SMOSops, thorough simulation studies are required.

In contrast with the multi-incidence angle concept, a future FPIR concept study at a fixed 50° incidence would benefit from the fact that, in a few months, MIRAS on SMOS will be launched. As such, collocations of MIRAS with several C-band + higher frequency fixed incidence angle (50°-55°) radiometers, such as Windsat and AMSR-E, will provide the opportunity to test for the first time the benefits of an FPIR-like instrument on MIRAS SSS retrievals with real data.

3.5 Spatial resolution

FPIR should ideally resolve the same spatial variability than MIRAS. The latter has a (variable) spatial resolution of 30-50 km. FPIR's preliminary design results in 100 km resolution at X-band. For the same instrument design and configuration, the spatial resolution ratio between C-band and X-band is about 1.5 (e.g., Windsat and AMSR-E). That is, keeping FPIR's current design, its spatial resolution is expected to be about 150 km at C-band. In contrast, at 37 GHz, FPIR's resolution would be about 30 km.

As such, MIRAS is able to resolve certain sea surface roughness variability that FPIR cannot resolve. When estimating FPIR's roughness retrieval error at 30-50 km scales, this unresolved variability is interpreted as a source of error, i.e., the representativeness error (Portabella and Stoffelen, 2009), which adds to FPIR's roughness retrieval error at 100 km (for X-band) or 150 km (for C-band) scales.

The estimation of the representativeness error is not straightforward. Stoffelen (1998) estimated a value of 0.75 m^2s^{-2} for the true sea surface wind component variance from scales of 50 km to 200 km in the extratropics. Based on this estimation, Portabella and Stoffelen (2009) assumed a representativeness error of 0.25 m^2s^{-2} in the tropics, where small-scale wind variability is expected to be generally smaller. According to Portabella and Stoffelen (2009), the representativeness error represents about 10% (20%) of the total error in the tropics (extratropics).

For FPIR-derived sea surface roughness at 30-50 km resolution (i.e., MIRAS spatial resolution), the representativeness error should represent smaller fractions of the total error than the ones indicated above, since the resolution gap for FPIR (about 100 km at C-band or 50 km at X-band) is smaller than the one accounted for in Stoffelen (1998), i.e., 150 km. In particular, a smaller representativeness error is obtained at X-band with respect to C-band.

4. Summary and recommendations

The main goal of this study is to determine the FPIR configuration, notably in terms of frequency, polarization, incidence angle, and resolution, which optimizes SMOSops SSS retrievals. For such purpose, a thorough review of the ability of past

and current passive microwave instruments to characterize the sea surface roughness is carried out.

To characterize the sea surface roughness scales resolved by the L-band MIRAS instrument, the (primary) FPIR frequency has to be close to L-band and have sufficient roughness sensitivity. These two requirements are met indeed by C and X bands. However, it is difficult at this time to conclude on whether C or X band is the optimal choice. C-band is about 20% less sensitive to sea surface roughness than X-band. However, X-band is almost twice as sensitive to atmospheric effects as C-band.

The third (U) and fourth (V) Stokes parameters can provide wind direction information. However, to accurately retrieve wind direction from U and V, several fully polarimetric frequencies are required. Moreover, ignoring the directional information has a generally small negative impact in the sea surface roughness retrieval at X or C band. This negative impact is smaller at C-band than at X-band, since the Tb_V and Tb_H sensitivities to wind direction decrease with decreasing frequencies. Alternatively, one can use auxiliary (NWP) wind direction information.

A dual frequency system is identified as an important requirement for disentangling surface roughness and atmospheric effects. Three different frequency combinations are considered: C + X, C + 37 GHz, and X + 37 GHz. C + X are least affected by atmosphere and provide sufficient roughness sensitivity. However, the 37 GHz channel can be used to optimally screen significant atmospheric "contaminated" data, and therefore ensure more accurate roughness estimation.

Due to the variety of MIRAS incidence angles (0°-60°), a multi-incidence angle FPIR system is considered. This system seems especially suitable when the roughness effect reduction method (see section 2.2) is used for SMOSops SSS retrievals. As shown by Reul et al. (2009), a measurement combination from different channels at 50° incidence angle can effectively reduce roughness effects while preserving SSS sensitivity, even though such channels are very little sensitive to SSS. However, there is no data available outside the 50°-55° incidence angle range to study and define the multi-incidence angle configuration.

With the current FPIR design, the spatial resolution of the instrument would be about 100 km at X-band and 150 km at C-band. The scales resolved by MIRAS but not by FPIR constitute an additional source of error to FPIR roughness estimation. The representativeness error is generally small although not negligible and less significant at X-band than at C-band.

We therefore recommend a dual frequency and dually polarized radiometer as FPIR-type secondary payload. However, the preferred frequencies and incidence angle configurations are still unclear.

With the launch of SMOS by September 2009, the first L-band MIRAS calibrated measurements are expected to be available in the beginning of 2010. As already mentioned, by collocating SMOS (L-band) data with AMSR-E or Windsat (X, C, K, and higher frequencies), one can better assess the optimal frequency configuration for FPIR on SMOSops. We therefore recommend a thorough study from the mentioned collocated data set before concluding on the FPIR frequency configuration.

Regarding the incidence angle configuration, all past and existing satellite radiometers have been configured at a fixed incidence angle of about 50°. As such, to look into the incidence angle issue either simulations or campaign data will be required.

Finally, it is unclear at this point whether the optimal SMOSops complementary instrument would be either an active system at L-band or a passive system at neighbouring bands like the one reported in this work. Since the upcoming American salinity mission, i.e., Aquarius (to be launched in 2010), will also carry an L-band scatterometer, we recommend to study the contribution of such active system to the characterization of surface roughness and the improvement of SSS retrievals and compare the results to the passive system collocation study (AMSR-E/Windsat) mentioned earlier.

Acknowledgments

References

Adams, I.S.; Hennon, C.C.; Jones, W.L.; Ahmad, K.A., "Hurricane wind vector estimates from WindSat polarimetric radiometer," *Proc. of IEEE Geoscience and Remote Sensing Symposium*, vol. 6, pp. 4014 – 4017, 25-29 July 2005.

Adams, I.S.; Hennon, C.C.; Jones, W.L.; Ahmad, K.A., "Evaluation of hurricane ocean vector winds from WindSat," *IEEE Trans. Geosci. Remote Sens.*, vol. 44 (3), pp. 656 – 667, 2006.

Bettenhausen, M.H., Smith, C.K., Bevilacqua, R.M., Wang, N., Gaiser, P.W., and S. Cox, "A nonlinear optimization algorithm for WindSat wind vector retrievals," *IEEE Trans. Geosci. Remote Sens.*, vol. 44 (3), pp. 597 – 610, 2006.

Camps, A., Corbella, I., Vall·llossera, M., Duffo, N., Torres, F., Villarino, R., Enrique, L., Julbé, F., Font, J., Julià, A., Gabarró, C., Etcheto, J., Boutin, J., Weill, A., Rubio, E., Caselles, V., Wursteisen, P., Martín-Neira, M. "L-band sea surface emissivity: Preliminary results of the WISE-2000 campaign and its application to salinity retrieval in the SMOS mission," *Radio Sci.,* 38 (4), 10.1029/2002RS002629, 2003.

Camps, A., Font, J., Vall-llossera, M., Gabarró, C., Corbella, I., Duffo, N., Torres, F., Blanch, S., Aguasca, A., Villarino, R., Enrique, L., Miranda, J., Arenas, J., Julià, A., Etchetto, J., Caselles, V., Weill, A., Boutin, J., Contardo, S. "The WISE 2000 and 2001 Field Experiments in Support of the SMOS Mission: Sea Surface L-Band

Brightness Temperature Observations and their Application to Multi-Angular Salinity Retrieval," *IEEE Trans. Geosci. Remote Sens.*, vol. 42, pp. 804-823, 2004.

Camps, A., Vall-llossera, M., Torres, F., Duffo, N., and Corbella, I., "Performance of Sea Surface Salinity and Soil Moisture Retrieval Algorithms with Different Ancillary Data Sets in 2D L-Band Aperture Synthesis Interferometric Radiometers," *IEEE Trans. Geosci. Remote Sens.*, vol. 43, pp. 1189-1200, 2005.

Camps, A., Vall-llossera, M., Villarino, R., Reul, N, Chapron, B., Corbella, I., Duffo, N., Torres, F., Miranda, J., Sabia, R., Monerris, A., and Rodríguez, R., "The Emissivity of Foam-Covered Water Surface at L-Band: Theoretical Modeling and Experimental Results from the FROG 2003 Field Experiment," *IEEE Trans. Geosci. Remote Sens.*, vol. 43, pp. 925-937, 2005.

Deblonde, G., "Evaluation of FASTEM and FASTEM-2," *NWP SAF Report*, available at http://www.metoffice.com/research/interproj/nwpsaf/rtm/, 2000.

English, S. J., and T. J. Hewison, "A fast generic millimetre wave emissivity model," *Microwave Remote Sensing of the Atmosphere and Environment Proc. SPIE* 3503, pp. 22– 30, 1998.

ESTEC, "Statement of work: SMOSops scientific support study (CCN-2 to SMOPSops), European Space Agency, Issue 1, May 2008.

Font, J., G. Lagerloef, D. Le Vine, A. Camps, and O.Z. Zanife, "The determination of surface salinity with the European SMOS space mission," *IEEE Trans. Geosci. Remote Sens.*, 42 (10), 2196-2205, 2004.

Freilich, M.H., Vanhoff, B.A., "The accuracy of preliminary WindSat vector wind measurements: comparisons with NDBC buoys and QuikSCAT", *IEEE Trans. Geosci. Remote Sens.*, vol. 44 (3), pp. 622- 637, 2006.

Gabarró, C., Portabella, M., Talone, M., and Font, J., "Towards an optimal SMOS ocean salinity inversion", *IEEE Geosci. Rem. Sens. Lett.*, accepted in January 2009.

Gentemann, C. L., Meissner, T., and Wentz, F. J., "Accuracy of satellite sea surface temperatures at 7 and 11 GHz," submitted to *IEEE Trans. Geosci. Remote Sens.*, February 2009.

Kudryavtsev, V., D. Hauser, G. Caudal, and B. Chapron, "Semiempirical model of the normalized radar cross-section of the sea surface," *J. Geophys. Res.*, 108(C3), 8054, doi:10.1029/ 2001JC001003, 2003.

Martín-Neira, M., and J.M. Goutoule, "A two-dimensional aperture-synthesis radiometer for soil moisture and ocean salinity observations, *ESA Bull.*, 92, 95–104, 1997.

Meissner, T., and Wentz, F. J., "An updated analysis of the ocean surface wind direction signal in passive microwave brightness temperatures," *IEEE Trans. Geosci. Remote Sens.*, vol. 40, no. 6, pp. 1230-1240, 2002.

Meissner, T., and Wentz, F. J., "Ocean retrievals for WindSat: radiative transfer model, algorithm, validation," *Proc. of the 9th Specialist Meeting on Microwave Radiometry and Remote Sensing Applications,* San Juan, Puerto Rico, 28 February – 03 March 2006, IEEE Catalog no. 06EX1174C, 2006.

Meissner, T., and Wentz, F. J., "Wind vector retrievals under rain with passive satellite microwave radiometers," submitted to *IEEE Trans. Geosci. Remote Sens.*, December 2008.

Monahan, E. C., and I. G. O'Muircheartaigh, "Whitecaps and the passive remote sensing of the ocean surface," *Int. J. Remote Sens.*, 7, pp. 627– 642, 1986.

Monaldo, F.M., "Evaluation of WindSat wind vector performance with respect to QuikSCAT estimates," *IEEE Trans. Geosci. Remote Sens.*, vol. 44 (3), pp. 638- 644, 2006.

Portabella, M., and Stoffelen, A., "On scatterometer ocean stress," *J. Atm. and Ocean Techn.*, **26** (2), pp. 368–382, 2009.

Quilfen, Y., C. Prigent, B. Chapron, A. A. Mouche, and N. Houti, "The potential of QuikSCAT and WindSat observations for the estimation of sea surface wind vector under severe weather conditions," *J. Geophys. Res.*, 112, C09023, doi: 10.1029/2007JC004163, 2007.

Reul, N., Saux-Picart, S., Chapron, B., Vandemark, D., Tournadre, J., and Salisbury, J., "Demonstration of ocean surface salinity microwave measurements from space using AMSR-E data over the Amazon plume," *submitted to Geophysical Research Letters*, February 2009.

Sobjaerg, S.S., Rotboll, J., and Skou N., "Wind effects and angular dependence at L-band polarimetric data: First results of LOSAC," In: *First Results Workshop on EuroSTARRS, WISE, LOSAC Campaigns*, Toulouse (France), November 2002, ESA SP-525, ISBN: 92-9092-835-2, ISSN: 0379-6566, 2003.

Soisuvarn, S., Jelenak, Z., and Chang, P.S, "A geophysical model function for windsat polarimetric radiometer wind retrievals using linear polarizations," *Proc. of IEEE Geoscience and Remote Sensing Symposium*, pp. 2523 - 2526, 23-28 July 2007.

Stoffelen, A., "Error modeling and calibration: Towards the true surface wind speed," J. Geophys. Res., 103 (C4), 7755–7766, 1998.

Yan, J., "FPIR: an X-band interferometer designed for operational SMOS," *Soil Moisture and Ocean Salinity workshop 2008*, Beijing, China, March 2008.

Yan, J., Wu, J., and Martín-Neira, M., "FPIR: A one dimensional full polarization interferometric radiometer," *IEEE Geoscience and Remote Sensing Symposium*, Barcelona, Spain, 23-28 July 2007.

Yueh, S., W. Wilson, S. Dinardo, and F. Li, "Polarimetric microwave brightness signatures of ocean wind directions," *IEEE Trans. Geosci. Remote Sens.*, vol. 37, pp. 949–959, 1999.

Yueh, S.H., Wilson, W.J., Dinardo, S.J., and Hsiao, S.V., "Polarimetric microwave wind radiometer model function and retrieval testing for WindSat," *IEEE Trans. Geosci. Remote Sens.*, vol. 44 (3), pp. 584 - 596, 2006.

Yueh, S.H., "Directional signals in Windsat observations of hurricane ocean winds," *IEEE Trans. Geosci. Remote Sens.*, vol. 46 (1), pp. 130 - 136, 2008.

Wentz, F. J., and Meissner, T., "Algorithm theoretical basis document for AMSR-E ocean algorithms: Supplement 1," RSS Technical Report 051707, 2007.

Zine, S., Boutin, J., Font, J., Reul, N., Waldteufel, P., Gabarró, C., Tenerelli, J., Petitcolin, F., Vergely, J.L., Talone, M. and Delwart, S. "Overview of the SMOS Sea Surface Salinity Prototype Processor," *IEEE Trans. Geosci. Remote*, vol. 46, no. 3, pp. 621–645, 2008.

SMOSops Scientific Support Study

Secondary Payloads Science Assessment – GNSS-R

1. Introduction

Global Navigation Satellite System-Reflections (GNSS-R) are signals of opportunity scattered by the Earth surface and suitable of being used in several remote sensing applications. They are free (already existing) and have a high-accuracy level that allows them to be detected by a space-borne passive instrument. Simultaneous reception of GNSS signals from different satellites allows a wide coverage and high temporal sampling over the oceans. Other advantages of this methodology are an increasingly larger global infrastructure with small and cheap system, and the long-term GNSS mission lifetime, which guarantees availability in future. The bistatic geometry of a GNSS-R remote sensing measurement is depicted in Fig. 1, in which the incoming and reflected rays of a signal transmitted by a GNSS satellite are shown.
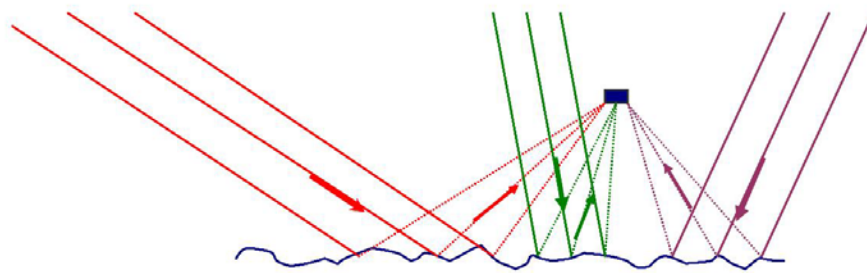
Fig. 1 Bistatic GNSS-R Geometry [Lowe, 2008]

At the beginning of the 90's, the PARIS (PAssive Reflectometry and Interferometry System) concept (Martin-Neira, 1993) is the first proposal of GNSS-R signals application to altimetry.

GNSS-R remote sensing has been performed by several platforms, spanning from ground measurements (Treuhaft et al., 2001; Belmonte-Rivas and Martin-Neira, 2006; Marchán, 2009), to airplanes (Garrison and Katzberg, 1998; Rius et al., 2002; Ruffini et al., 2004), stratospheric balloons (Cardellach et al., 20039, and spacecraft (Lowe et al., 2002; Cardellach et al., 2004; Gleason et al., 2005).

A broad range of applications have been devised and can be grouped into altimetry, sea state/roughness, sea ice, soil moisture, sea surface salinity. Several institutions have been involved in the above mentioned activities, among them: JPL/Caltech, Purdue University and Colorado State University in USA, SSTL (Surrey) and NOCS (National Oceanography Centre, Southampton) in UK, CLS and IFREMER in France, Starlab, IEEC (Institut d'Estudis Espacials de Catalunya), and more recently (since 2002), UPC in Spain.

2. Theoretical Framework and Modelling

The physical mechanisms behind the observed signal scattering have been deeply studied. A widely-used model based on the Kirchhoff approximation and Geometric Optics (GO) limit was formulated by Zavorotny and Voronovich (1999), (Z-V model) and is often used in conjunction with the ocean wave spectrum developed by Elfouhaily et al. (1997) in order to explain the observed behaviour of ocean scattered GNSS signals.

The ocean wave spectrum model developed by Elfouhaily and his colleagues is currently believed to be the best representation of the ocean waves for the GNSS bistatic problem. It is defined by the electromagnetic wave number and the wind speed in the following formulation:

$$\Psi(k, U_{10}, \varphi) = \frac{1}{2\pi} k^{-4} \left[B_l(U_{10}) + B_h(U_{10}) \right] \left[1 + \Delta(k, U_{10}) \cos(2\varphi) \right] \tag{1}$$

The outputs of the Elfouhaily wave spectrum are used as inputs into the Z-V scattering model. The wave number elevation spectrum shown above is converted to a wave number wave slope spectrum; by integrating such spectrum over all the wave numbers and the wave directions it is possible to calculate the omni-directional mean square wave slope (*mss*):

$$mss(U_{10}) = \int_0^{k^*} \int_{-\pi}^{\pi} k^2 \Psi(k, U_{10}, \varphi) d\varphi dk \tag{2}$$

The wave number integration cut-off k^* was initially estimated as:

$$k^* = \frac{1}{3} k = \frac{2\pi}{3\lambda} \tag{3}$$

by Zavorotny and Voronovich (2000), where λ is the incident wavelength. Subsequently Garrison et al. (2002) proposed

$$k^* = \frac{2\pi \cos(\theta)}{3\lambda} \tag{4}$$

where θ is the reflection incidence angle.
Later, Thompson et al. (20059 suggested an improved cut-off which was also dependant on the wind speed. The resulting cut-off was empirical:

$$k^* = \frac{2\pi \cos(\theta)}{15\lambda} \left(1 + \frac{U_{10}}{20} \right) \tag{5}$$

Eventually, the relationship between the *mss* and the 10-m wind speed using the Elfouhaily spectrum is described in Fig. 2
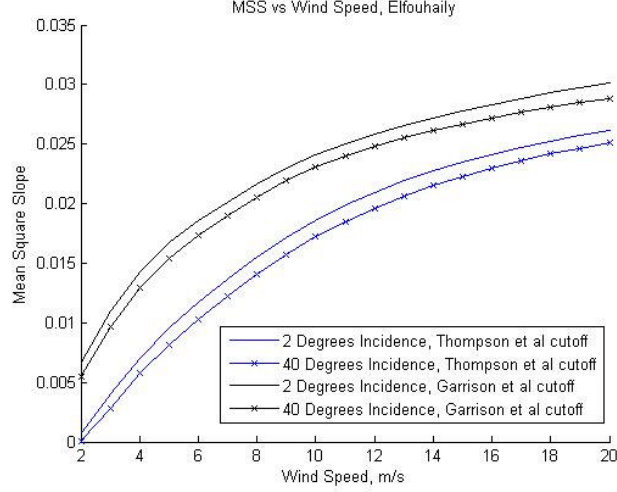
Fig. 2 Mean square slopes versus 10-m wind speed, at different cut-off wave number and incidence angle [from Gleason, 2006]

The mean square slope represents the variance of the ocean surface slope distribution that is used to generate the probability density function (PDF) of the surface slopes and which is related to the bistatic radar cross section (BRCS) as:

$$\sigma^0 = X \cdot P \tag{6}$$

where X is a scaling coefficient and P is a wave slope PDF. The BRCS is thus a function of the dielectric properties of seawater and the PDF of the surface slopes. A specific distribution gives information on the backscattered signal which is captured by the receiver. Ocean waves rarely comply with a perfect Gaussian distribution. Often, waves are sharper at their peaks and are known to lean slightly in the direction the wind is blowing. Small amounts of kurtosis and skew in the observed wave slope probability distributions have also been observed.

At each specific time-delay and frequency-cut, a waveform model can be derived according to the aforementioned formulation of Zavorotny-Voronovich (Z-V scattering model). The final expression for the scattered signal power of a GPS signal is summarized below:

$$Y_s\left(\hat{\tau}, \hat{f}\right) = \frac{T_I^2 P_T \lambda^2}{(4\pi)^3} \iint_A \frac{G_T \sigma^0 G_R}{R_R^2 R_T^2} \Lambda^2\left(\hat{\tau} - \tau\right) \mathrm{sinc}^2\left(\hat{f} - f\right) dA \tag{7}$$

For a more detailed description of the different terms, see Zavorotny and Voronovich (2000). The Z-V representation above is based on geometric optics and excludes all Bragg scattering effects, assuming only diffuse scattering from the ocean surface. It has to be said that the Z-V model requires two assumptions. The first assumption is the Kirchhoff approximation which applies the condition that the scattering surfaces are planar with no multiple surface reflections occurring. The second is the geometric optics limit of the Kirchhoff approximation which assumes, for sufficiently rough surfaces (wind speeds > 2m/s), that only waves of favourable orientations will contribute to the scattered power.

The BRCS is the primary source of uncertainty in the Z-V model; the scattering cross section depends to a large extent on the surface roughness and the wavelength of the incident radiation.

3. GNSS-R Observables

A model such as the Z-V can be used to generate delay waveforms and delay Doppler maps (described later on) using inputs of sea surface slope statistics, once receiver and transmitter geometries are properly taken into account.

Figure 3 describes the transmitter/receiver configuration, illustrating the specular reflection point and the surrounding so-called "glistening zone", the roughened zone which produces the backscattered signals detected by the receiver.
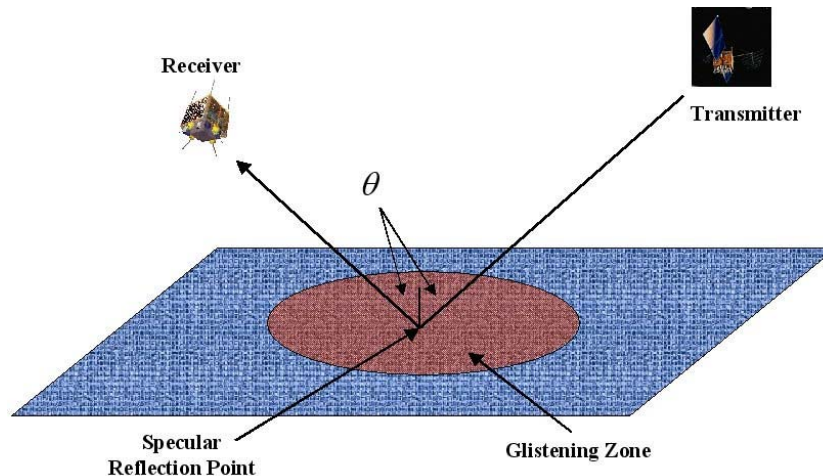

Fig. 3 Schematic configuration showing the specular point and the glistening zone [Gleason, 2006]

The size of the glistening zone will depend on the roughness of the surface and increase as a function of incidence angle. Consequently, the power can scatter off a very large ocean surface, usually well over tenths of kilometres. As can be seen, at each point in the glistening zone, the path delay and reflection angles are different. This results in a range of different path delays (between the transmitter and receiver) and Doppler frequencies at the receiver, due to the relative motion.
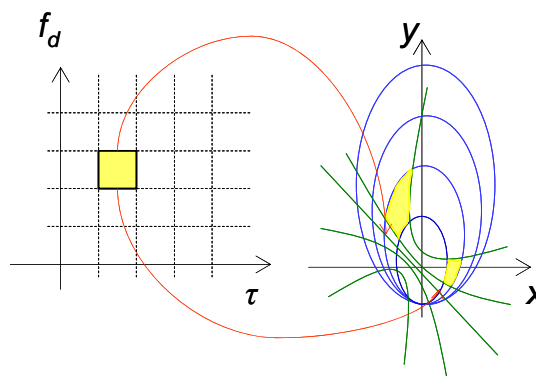
Fig. 4. A specific cell at a certain delay and at specific Doppler frequency represented by iso-range ellipses and iso-Doppler parabolas in the 2D spatial domain [Marchán, 2009].

In Fig 4 it is shown how a specific cell of a certain time delay and at specific Doppler frequency in the time-frequency domain is represented in the bi-dimensional plane of the surface backscattering. Lines of equal delay across the surface (or iso-range lines) can be drawn as ellipses centred at the point of specular reflection. Lines of constant

frequency result in parabolic shaped iso-Doppler lines cutting through the glistening zone.

As the signal scatters, the time delay and the frequency of the received signals change; where narrowly spaced iso-range ellipses and iso-Doppler parabolas can be mapped across the Earth. Figure 5 shows an example at different incidence angles.
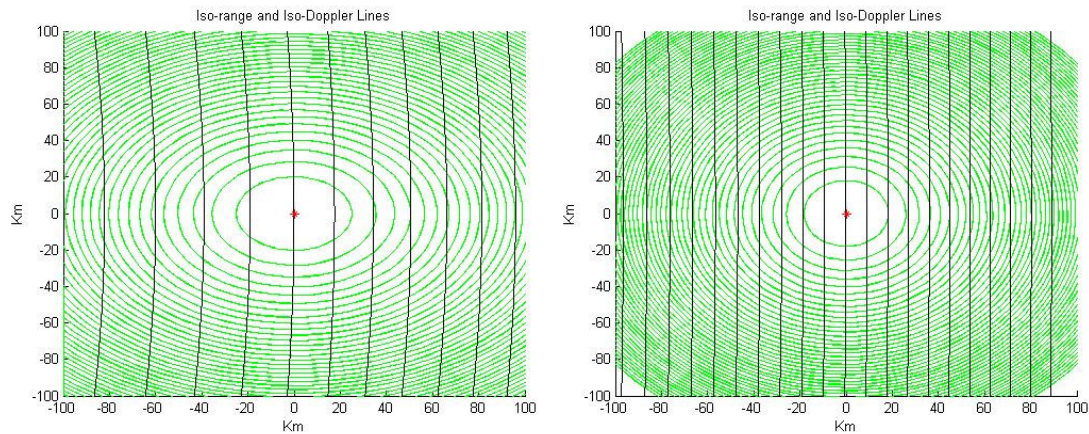

Fig. 5 Iso-range and iso-Doppler fields at different (10 degrees and 40 degrees) incidence angle [from Gleason, 2006].

Main GNSS-R observables are
- Peak Amplitude
- Delay Map: received power at several delay bins
- Delay-Doppler Map (DDM): received power spread over a range of different delays and frequencies

In Figure 6 several waveforms at specific time delays (expressed in chips) as a function of the different wind speeds are shown. A delay waveform is the returned power profile as a function of delay only, with the frequency set to a constant value (in general, the value at the specular point). A single L1 C/A code chip represents approximately 300 meters in delay, or one microsecond.
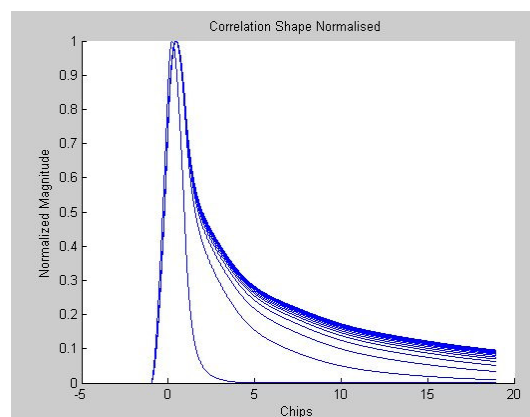

Fig. 6 Delays waveforms, at different wind speeds [Gleason, 2006]

A bi-dimensional representation of the power distribution all over an ocean surface with respect to a specular point is shown, in turn, in Fig. 7.
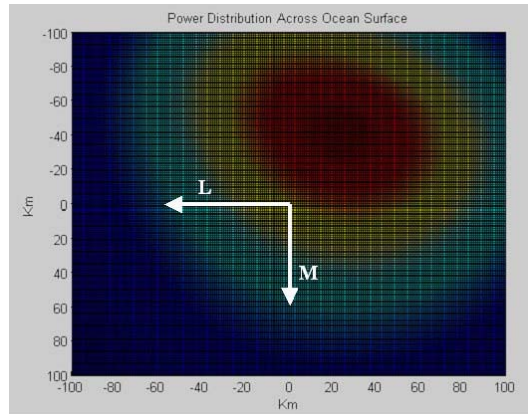
Fig. 7 The scattering power distribution over the spatial glistening zone [Gleason, 2006]

The signal power can be mapped as a function of frequency and delay together to produce a delay-Doppler map, or a wide area delay/frequency mapping of the received power (Fig. 8). Remote sensing of the ocean surface is performed by estimating as accurately as possible the extent and shape of the glistening zone with all non-ocean related distortions to the signal power corrected for.
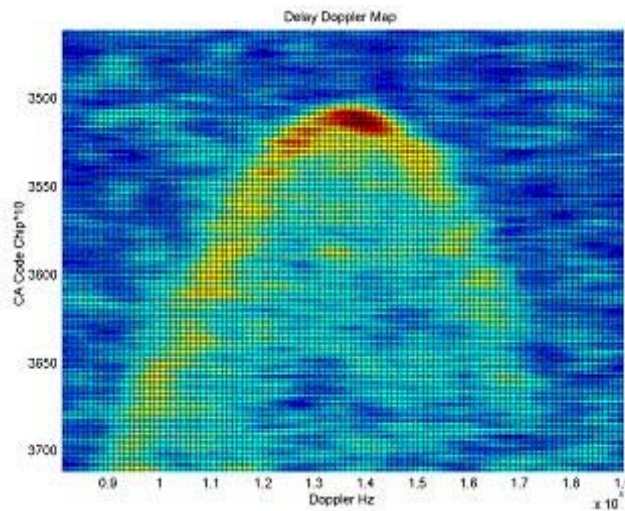

Fig. 8 Representation of a Delay-Doppler map at different Doppler and time-delays [Gleason, 2006]

4. SMOSops Estimated Coverage and Accuracy

In Fig. 9 the number of expected reflections that would be collected by a hypothetic receiver onboard the future SMOSops satellite is shown, considering all the reflections produced by the different constellations: the US Global Positioning System (GPS), the European forthcoming Galileo system, and the geostationary augmentation system. On average, it is estimated that roughly 60 transmitters will be simultaneously available (D'Addio, 2008).

For an orbit height of 800 km and a corresponding swath of 1300 km, on average 4 specular points per each single GNSS constellation are collected, with a sampling rate roughly 16 times higher than, for instance, conventional radar altimeters.
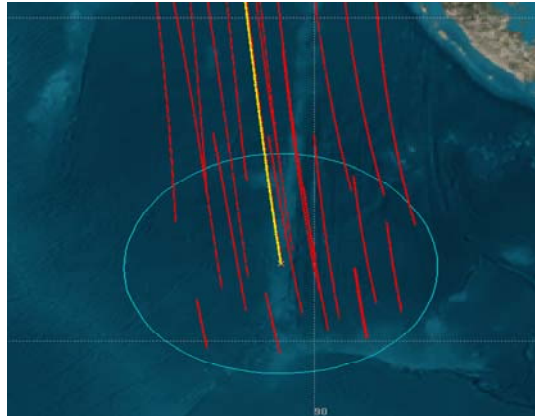
Fig. 9 Expected reflections collected by the future SMOSops receiver by considering different constellations [D'Addio, 2008].

With regard to the future SMOSops GNSS-R instrument accuracy, according to De Vos and Steenwijk (2009) SSTL (Surrey Satellite Technology Limited) Technical Note, the scattering cross section of the reflection point can be estimated by properly combining the SNR (Signal to Noise Ratio) of both direct and reflected GNSS signals. The estimated accuracy of the scattering cross section is 1.2 dB. One way to gather insights on the implications of such accuracy in the performances of the instrument (and thus in the salinity retrieval) is to relate such uncertainty to the corresponding uncertainty in brightness temperature at L-band.

In Narayan et al. (2006) L-band radar backscattering coefficients using the NASA/JPL airborne synthetic aperture radar (AIRSAR, Yunling et al., 2004) are combined with L-band radiometric data obtained by PALS (Passive and Active L- and S-band sensor, Wilson et al., 2001) in coincident datasets acquired during the SMEX02 campaign. In Fig. 10 the good correlation between the L-band VV channel AIRSAR backscattering coefficients change and the corresponding change in PALS L-band V channel brightness temperatures is illustrated.
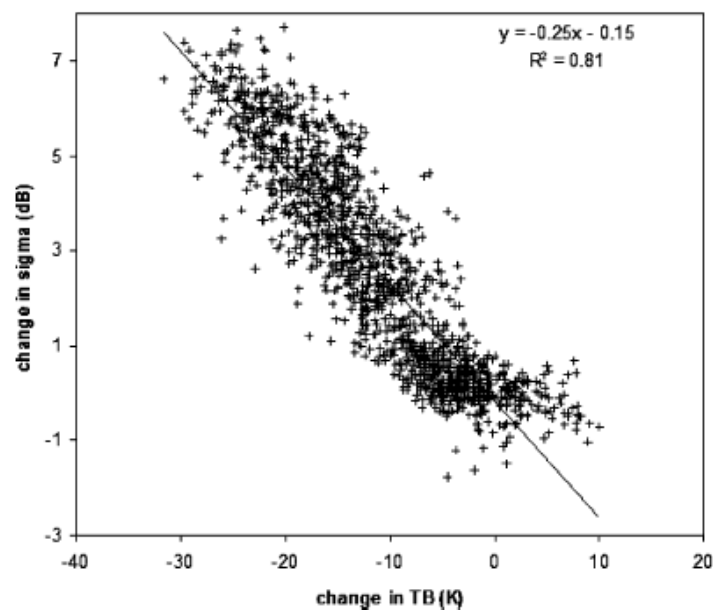

Fig. 10 Change in L-band AIRSAR backscattering coefficients plotted versus change in L-band PALS data brightness temperature, showing the regression line and the correlation coefficient [Narayan et al., 2006].

According to the figure, an uncertainty of 1.2 dB translates into an uncertainty in T_B of 4.8 K, which is too large to allow a reliable sea surface roughness correction, when applied to the salinity retrieval problem. Further investigation will be needed, both on the expected improvements in the instrumental performances and on the reliability of a relationship $\Delta\sigma_0 / \Delta T_B$ at L-band such that one just illustrated.

5. Salinity-related Impact Study

The use of GNSS signals reflected over the sea surface is a compelling yet challenging approach to describe roughness at a frequency close to SMOS. In the previous sections, the limitations of a fully theoretical approach have been described, showing how the present algorithms are not able yet to uniquely identify the relationship between the observed variable and the measured one.

Nevertheless, it has been proposed that the mean square slope that could be derived from GNSS-R signals could be a proper sea state descriptor and could be used to make the necessary sea state T_B corrections to improve the SSS estimates. In Sabia et al. (2007), a study using GNSS-R signals specifically in the SMOS framework has been performed, and the approach and the main results are summarized hereafter.

A hypothetical companion satellite equipped with a GNSS-R receiver flying in formation with SMOS could provide sea surface roughness estimates through the *mss* measurements. Since these measurements are not available, they have been derived from the existing relationship between *mss* and wind speed. The objective is that spatial and temporal collocation of these measurements could improve or complement the quality of the salinity retrieval, providing a preliminary assessment of the potential application of GNSS-R signals in the framework of the SSS retrieval.

The work was divided into three main parts: firstly, the determination of the relationship between the *mss* and the wind speed. Later, the description of the simulation results concerning the use of the GPS constellation alone. Afterwards, the extension of the study including other constellations suitable to be sources of GNSS-R opportunity signals.
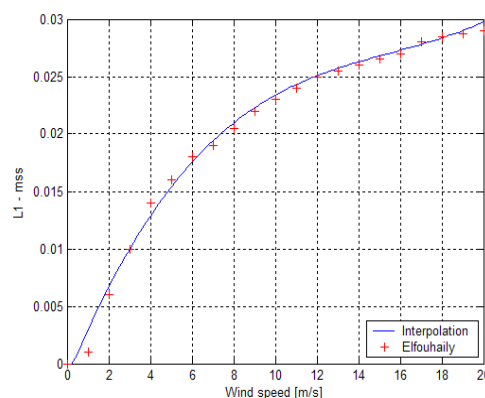

Fig. 11 The *mss* computed for the L1 GPS frequency as a function of wind speed (at λ=19 cm).

Concerning the simulation strategy, the main steps were the following: generation of the brightness temperatures in a selected test zone, computation of the specular points within the zone, identification of the empirical non-linear *mss*(U10) relationship, geolocation and association of the derived *mss* values, and SSS retrieval scheme definition with GNSS-R auxiliary data.

Figure 11 shows the relationship between the wind speed and the mean square slope as it was used in this study. This allowed the replacement of wind speed parameter by the *mss* data in the salinity retrieval cost function.

To exploit the capabilities of the GNSS-R derived data in characterizing the sea state, simulations have been performed at increasing complexity, firstly by using only the specular points calculated by means of the GPS constellation alone, and then by adding the following constellations: the Russian GLONASS, the future European GALILEO, and the Satellite Based Augmentation Systems (SBAS)/INMARSAT telecommunications satellites in geostationary orbit. The theoretical companion satellite would fly in two configurations; firstly, in formation side-by-side with SMOS, and then as a tandem satellite flying 500 km behind the SMOS payload in the same orbit. Thus, the overall setup of simulations consisted of four constellations, in two configurations with respect to SMOS, for the two instrument operation modes (Th and Tv measured in fully polarimetric mode or *I* measured in dual-polarization mode) and for both satellite passes (ascending and descending). This setup resulted in 32 single-constellation simulations. Subsequently, to use as many specular reflection points as possible, a merging of the results from the previous simulations provided the final assessment of this study. The specular points of the different constellations in both configurations exhibit a wide range of variability in their occurrence in the days considered.
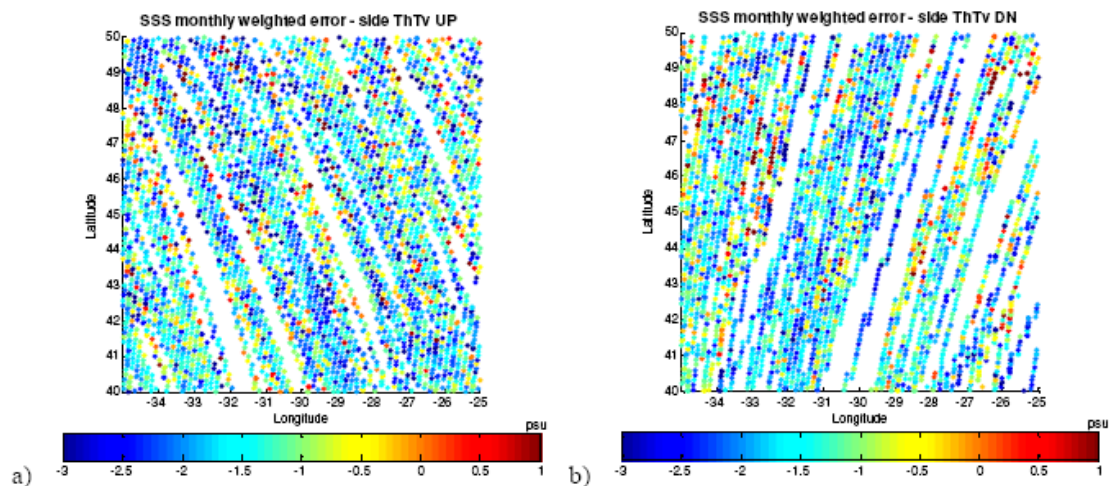

Fig. 12 Monthly weighted errors relevant to specular points for multiple blended constellations in full-pol mode for a) side configuration, ascending pass b) side configuration, descending pass

All the single-overpass SSS retrievals at the pixel level in the different configurations have been merged to obtain a blended retrieval for each day, and then monthly averaging has been performed. The single-overpass Level 2 SSS values are firstly temporally-averaged in a single grid cell. This is performed with a weighting procedure which takes into account the pixel position in the SMOS FOV in each single overpass, giving less weight to the noisy observations away from the central track. Therefore, these monthly-averaged pixels are spatially-averaged in a 2°x2° grid.

The distribution of the corresponding error in the selected 10º test zone provides the retrieval performances, which are reported as bias (mean value), accuracy (standard deviation) (Sabia, 2009). Figures 12a and 12b show the monthly weighted errors in the "side" configuration cases for fully polarimetric mode, emphasizing the inhomogeneous sampling in the different configurations.

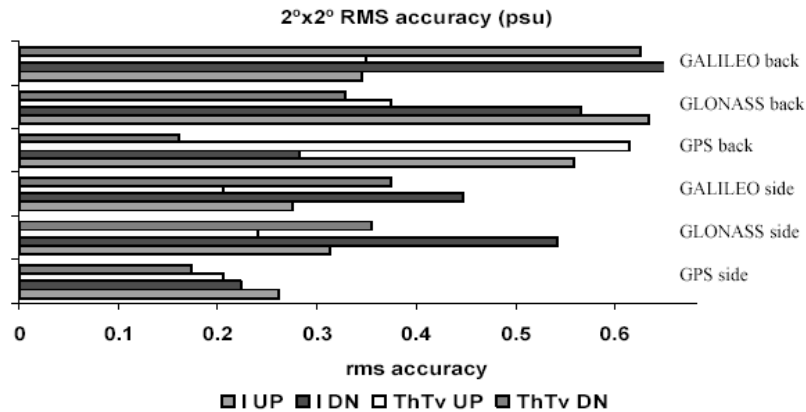Figure 13 shows the L3 salinity accuracy by using all the constellations in the different configurations chosen.

Fig. 13 2°x2° spatially-averaged salinity accuracy for the different constellations and configurations studied, for both polarimetric mode and satellite passes (indicated in the legend below).

Limitations and achievements of this study are summarized below:

Limitations:
 • Limited number of GNSS specular reflection points
 • Large uncertainty in the sea state parameterization

Achievements:
 • Multiple GNSS constellations retrieval accuracy is comparable to retrieval using auxiliary winds different from the original
 • Spatio-temporal collocation of the measurements

Potential Improvements by using a larger Glistening zone are envisaged. That is, considering reflections not only in the exact moments when the specular reflections take place, but within a narrow temporal window in which the roughness can be assumed to remain unchanged. The number of available *mss* points will thus be increased, and better results should be expected.

6. Empirical methodology

Besides the GNSS-R modellizations efforts previously described, another option that should be considered aims at exploiting the semi-empirical relationships between the brightness temperatures and some specific GNSS-R-derived variable. In Marchán et al. (2008) it is proposed to use a GNSS-R data processing method that involves the Area and Volume of the normalised Delay-Doppler Maps (DDMs). The Volume of a normalized (to the maximum value) DDM can be determined as:

$$Volume = \int_{\tau_{min}}^{\tau_{max}} \int_{f_{d,min}}^{f_{d,max}} \overline{DDM}(\tau, f_d) \cdot d\tau \cdot df_d \tag{8}$$

where τ_{min}, τ_{max}, $f_{d,min}$, $f_{d,max}$ are the minimum and maximum values for the delay offset and Doppler shift, respectively. The Area of a specific section of the normalized DDM can be derived as follows:

$$Area = \underset{\overline{DDM}(\tau, f_d) > threshold}{\iint} d\tau \cdot df_d \tag{9}$$

whereas the threshold is defined at a percentage of the maximum, namely, considering the values over a chosen signal amplitude.

In Fig. 14 the Volume and the Area of the normalized DDM are plotted versus the wind speed, ranging from 3 to 14 m/s, at different thresholds.
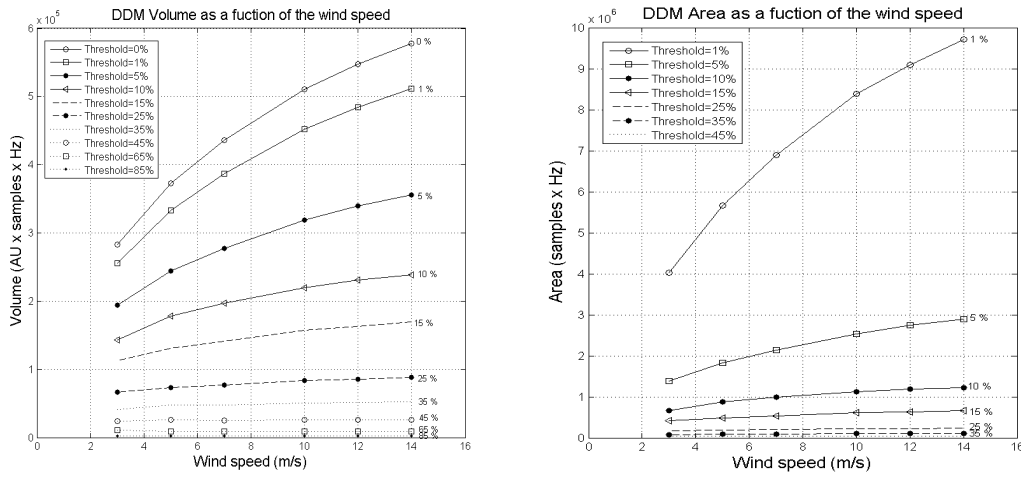

Fig. 14 Vol/Area of the normalized DDM as function of U_{10} [Marchán et al., 2008]

Both Volume and Area increase at increasing roughness, parameterized here only as function of wind speed, being larger the regions from which the signals are scattered. The lower the thresholds, the higher the sensitivity of Volume and Area to the wind speed.

Therefore, the choice of these observables (directly extracted from the DDMs) allows the derivation of a direct relationship with the roughness-induced T_B changes ΔT_B, according to:

$$T_{Bpol}(\theta) = T_{Bpol,flat\,sea}(\theta, f, SSS, SST) + \Delta T_{Bp}(\theta, \vec{p}) \tag{10}$$

Although DDMs' shape and T_B are also affected by other sea state descriptors ($\vec{p}$), such as *mss* and Significant Wave Height (SWH), the ΔT_B in this study has been related to wind speed through the SPM/SSSA method (Johnson and Zhang, 1999) using the Elfouahily (1977) sea spectrum (Fig. 15).
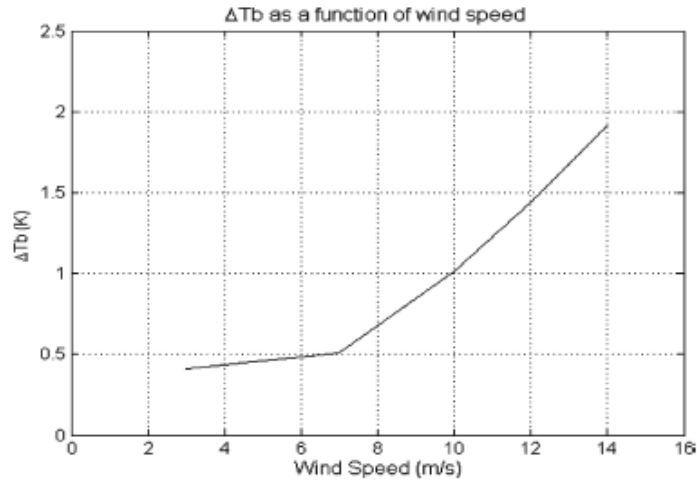
Fig. 15 ΔT_B at nadir as a function of the wind speed.

The computation of the wind speed-derived brightness temperature changes allow the direct comparison of the latter with the measured observables, that is Volume and Area, as it is shown in Fig. 16.
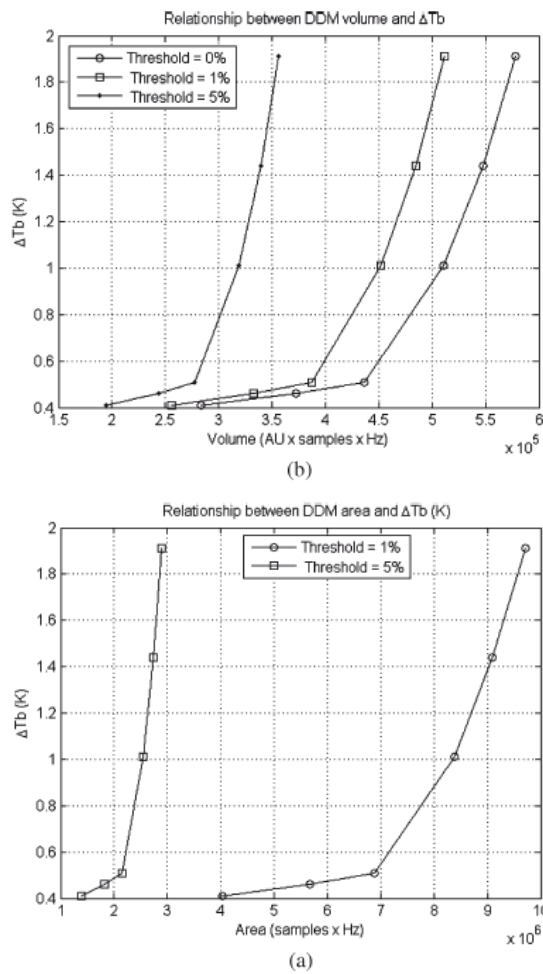

Fig. 16 ΔT_B as function of the Vol/Area of the normalized DDM [Marchán et al., 2008]

The relationship existing between the ΔT_B and the Volume/Area of the normalized DDM will only be correctly estimated once DDMs and T_Bs are simultaneously

measured, although in this study this relationship has been studied by means of the intermediate step of the derivation of the T_B sensitivities to the wind speed. In order to acquire simultaneously T_Bs and DDMs a field campaign took place in the summer of the 2008.

7. Measurements campaign (ALBATROSS 2008)

The Advanced L-BAnd Transmission and Reflection Observation over the Sea Surface (ALBATROSS) field experiment took place to rehearse a future SMOS Cal/Val activity between the months of May and July 2008, looking at an ocean zone within the Atlantic Subtropical Gyre, namely at the Mirador de la Aldea (Aldea de San Nicolás, Gran Canaria Island, Spain).

The aim was the simultaneous collection of brightness temperatures and GNSS-R over an ocean test zone off the NW coast of the island. Brightness temperatures are collected by means of the UPC L-band Automatic Radiometer (LAURA), while the sea surface GNSS-R under several sea-roughness conditions were measured using a GPS Reflectometer (PAU-GNSSR) whose glistening zone at 30º elevation was 140m x 280m at U_{10}= 5 m/s or 200m x 400m at U_{10} = 15m/s (Figs. 17 and 18).

Ground-truth measurements were obtained by 2 SSS/SST buoys from UPC and the Universidad de Las Palmas de Gran Canaria (ULPGC); 1 directional spectrum Triaxys instrument from UPC and 1 Waverider buoy from *Puertos del Estado* (the Spanish Ports administration). Several different sea conditions have been observed, with the wind speed taking values between 0 and 10 m/s, SST varying from 20 °C to 21.6 °C, with an average excursion of 1°C during day, and an approximately constant SSS of 36.8 psu.

Fig. 17 The PAU (Passive Advanced Unit) GNSS-R receiver and the instruments deployed, pointing at the test zone in which the buoys were moored to obtain ground-truth data.

The measured LAURA radiometer T_Bs were strongly contaminated by the soil emissivity picked up over the steep 360m cliff (where both the instruments were mounted).

The processing meant to filter the flat T_B component in order to get rid of the soil contribution and relate the T_B rough component only with the wind speed fields (registered simultaneously with the buoys available). Final assessment of the results is still ongoing and will benefit from the planned future field experiments in 2009.
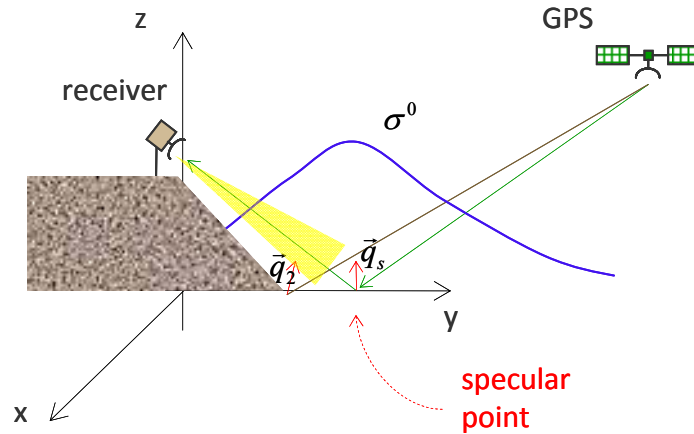

Fig. 18 Schematic view of the measurements setup, indicating the GNSS-R receiver (in the same position of the LAURA radiometer), collecting reflections of the GNSS constellation in an ocean surface portion lying down the cliff.

The final purpose is to directly relate this additional T_B term due to the wind speed with the DDM extracted by the GNSS-refelctometer instrument mounted onsite (whose data were processed in parallel).

Should this be possible, the relationship between the normalized DDM Volume and Area and the ΔT_B would be calculated empirically with ground-truth measurements. This would advance in addressing the link between generation of DDMs and geophysical effects determining the sea state/roughness. Preliminary processing exhibits a dependence of the Volume of the normalized DDM with SWH and *mss* as shown in Fig. 19.
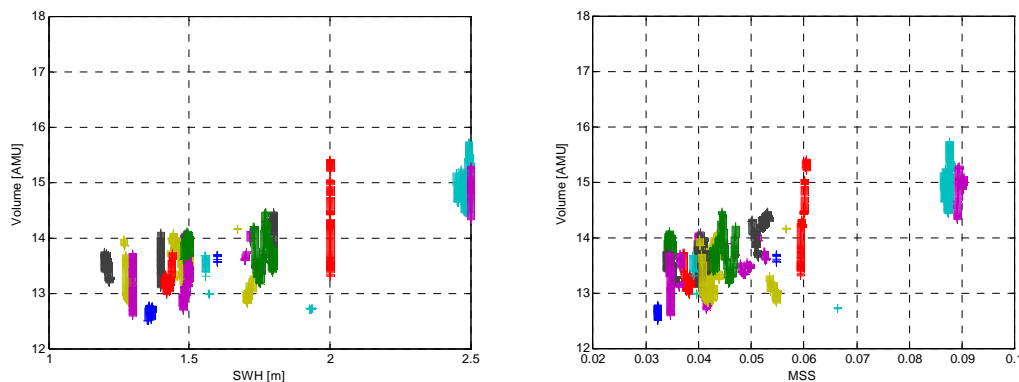

Fig. 19 The preliminary results of the calculated relationships between either the SWH or the *mss* with the Volume of the normalized DDM showing linear trends in both comparisons. [Marchán, 2009]

Follow-on of this field campaign is foreseen for the months of June/July 2009 in the same place and with additional instrumentation.

8. Conclusions

Despite the GNSS-R concept is a very promising technique to infer information on the sea state, the lack of modelling capabilities prevents from obtaining a unique formulation that relates the scene parameter with the observed measured variable. The concept can be addressed either form a theoretical or from a semi-empirical point of view, as it has been shown in this report. Relevant conclusions are summarised below.

- GNSS-R is a promising technique to be applied in the secondary payload of the future SMOSops mission, but further assessment of the physics underneath is still needed
- Direct relationship of T_B(mss) will suffer from the same weakness as other auxiliary data used in SMOS today, since the relationship between sea state and *mss* relies on sea surface spectrum descriptors and numerical models, both prone to errors and inaccuracies.
- Large international effort in the GNSS-R community are focused on:
    - Theoretical modelling
    - Empirical modelling
    - Hardware technology improvement
    - Data processing
- GNSS-R DDM empirical processing has the potential to improve the radiometric SSS retrieval
- Further applications (sea ice and SM) are suitable to provide insights in the determination of other parameters associated to SMOS

References

Belmonte-Rivas, M. and M. Martin-Neira, "Coherent GPS Reflections from the Sea Surface," IEEE Geosci. Remote Sensing Lett, 3 (1), 28–31, 2006.

Cardellach, E., G. Ruffini, D. Pino, A. Rius, A. Komjathy, and J.L. Garrison, "Mediterranean Balloon Experiment: Ocean Wind Speed Sensing from the Stratosphere Using GPS Reflections," Remote Sens. Environ., 88 (3), 351-362, 2003.

Cardellach, E., Ao, C.O., de la Torre-Juàrez, M., and Hajj, G.A., "Carrier phase delay altimetry with GPS-reflection/occultation interferometry from Low Earth Orbiters," Geophysical Research Letters, 31(10), May 2004.

D'Addio S., C. Buck and M. Martin-Neira, "GNSS-R Geometry and Coverage," GNSS-R 08 Workshop, ESA-ESTEC, Noordwijk, the Netherlands, September, 2008.

De Vos, R. and V. Steenwijk, "SMOSops GNSS-R Calibration Technical Note", October, 2008.

Elfouhaily, T., B. Chapron, K. Katsaros, and D. Vandermark, "A Unified Directional Spectrum for Long and Short Wind-driven Waves," J. Geophys. Res., 102 (7), 15781–15796, 1997.

Garrison, J.L., and J.L. Katzberg, "Effects of Sea Roughness on Bistatically Scattered Range Coded Signals from the Global Positioning System," Geophys. Res. Lett., 25 (13), pp, 1998.

Garrison, J.L., A. Komjathy, V.U. Zavorotny, and S.J. Katzberg, "Wind Speed Measurement Using Forward Scattered GPS Signals," IEEE Trans. Geosci. Remote Sens., 40 (1), 50 - 65, 2002.

Gleason, S., S. Hodgart, S. Yiping, C. Gommenginger, S. Mackin, M. Adjrad, and M. Unwin, "Detection and Processing of Bistatically Reflected GPS Signals from Low Earth Orbit for the Purpose of Ocean Remote Sensing," IEEE Trans. Geosci. Remote Sens., 43 (6), 1229–1241, 2005.

Gleason, S., "Remote Sensing of Ocean, Ice and Land Surfaces Using Bistatically Scattered GNSS Signals From Low Earth Orbit," Ph.D. Thesis, December, 2006.

Johnson, J.T., and M. Zhang, "Theoretical Study of the Small Slope Approximation for Ocean Polarimetric Thermal Emission," IEEE Trans. Geosci. Remote Sens., 37 (5), 2305-2316, 1999.

Lowe, S., J. LaBrecque, C. Zuffada, L.J. Romans, L.E. Young, and G.A. Hajj, "First Spaceborne Observation of an Earth-reflected GPS signal," Radio Sci., 37 (1), 1007, 2002.

Lowe, S., "Basic Principles of GNSS-R," GNSS-R 08 Workshop, ESA-ESTEC, Noordwijk, the Netherlands, September, 2008.

Marchan J.F., N. Rodriguez, A. Camps, X. Bosch, I. Ramos and E. Valencia, "Correction of the Sea State Impact in the L-band Brightness Temperature by means of Delay-Doppler Maps of Global Navigation Signals Reflected over the Sea Surface," IEEE Transactions on Geoscience and Remote Sensing, Vol. 46 (10), October 2008.

Marchán, J.F., "Sea state determination using GNSS-R techniques: contributions to the PAU instrument," Ph.D. Thesis, May, 2009.

Martín-Neira, M., "A Passive Reflectometry and Interferometry System (PARIS): Application to Ocean Altimetry," ESA Journal, 17, 331-355, 1993.

Narayan U., L. Venkataraman and T. J. Jackson, "High-Resolution Change Estimation of Soil Moisture Using L-Band Radiometer and Radar Observations Made during the SMEX02 exxperiments," IEEE Transactions on Geoscience and Remote Sensing, Vol. 44 (6), June 2006, pp. 1545-1554.

Rius, A., J.M. Aparicio, E. Cardellach, M. Martín-Neira, and B. Chapron, "Sea Surface State Measured Using GPS Reflected Signals," Geophys. Res. Lett., 29 (23), 2002.

Ruffini, G., F. Soulat, M. Caparrini, O. Germain, and M. Martin-Neira, "The Eddy Experiment: Accurate GNSS-R Ocean Altimetry from Low Altitude Aircraft," Geophys. Res. Lett., 31 (21), 2004.

Sabia R., M. Caparrini, A. Camps, and G. Ruffini, "Potential Synergetic Use of GNSS-R Signals to Improve the Sea State Correction in the Sea Surface Salinity Estimation: Application to the SMOS Mission," IEEE Transactions on Geoscience and Remote Sensing, Vol. 45 (7), July 2007, pp. 2088-2097.

Sabia, R., "Sea surface salinity retrieval error budget within the ESA Soil Moisture and Ocean Salinity mission," Ph.D. Thesis, October, 2008.

Thompson, D.R., T.M. Elfouhaily, and J.L. Garrison, "An Improved Geometrical Optics Model for Bistatic GPS Scattering from the Ocean Surface," IEEE Trans Geosci. Remote Sens., 43 (12), 2810-2821, 2005.

Treuhaft, R.N., S. Lowe, C. Zuffada and Y Chao, "2-cm GPS Altimetry Over Crater Lake," Geophysical Research Letters, Vol.22, No. 23, December 2001.

Wilson, W.J., S.H. Yueh, S.J. Dinardo, S.L. Chazanoff, A. Kitiyakara, F.K. Li, and Y Rahmat-Samii, "Passive active L- and S-band (PALS) microwave sensor for ocean salinity and soil moisture measurements," IEEE Transactions on Geoscience and Remote Sensing, Vol. 39 (5), May 2001, pp. 1039-1048.

Yunling, L., K. Yunjin, and J. van Zyl, "The NASA/JPL Airborne Synthetic Aperture Radar System,". [Online at http://airsar.jpl.nasa.gov/documents/genairsar/airsar_paper1.pdf].

Zavorotny V.U. and A.G. Voronovich, "Bistatic Radar Scattering from an Ocean Surface in the Small Slope Approximation," Proceedings of the IEEE International Geoscience and Remote Sensing Symposium 1999. Vol. 5, pp. 2419-2421. Hamburg, Germany, 1999.

Zavorotny V.U. and A.G. Voronovich, "Scattering of GPS Signals from the Ocean with Wind Remote Sensing Application," IEEE Transactions on Geoscience and Remote Sensing, Vol. 38, pp. 951-964, March 2000.